Sound & Vibration 2026, 60(1), 3765.
doi: https://doi.org/10.59400/sv3765

Article

Simulation modeling of fiber optic sensor subsystem for force and temperature measurement embedded in composite materials

Murat Kunelbayev[1,2], Aliya Kalizhanova[1,3], Ainur Kozbakova[1,4], Feruza Malikova[4,*], Timur Kartbayev[5]

[1] Institute of Information and Computational Technologies CS MSHE RK, Almaty 050010, Kazakhstan
[2] Department of Artificial Intelligence and Big Data, Al-Farabi Kazakh National University, Almaty 050040, Kazakhstan
[3] Department of IT Engineering and Artificial Intelligence, Almaty University of Energy and Communications named after G. Daukeyev, Almaty 050013, Kazakhstan
[4] Department of Information Systems, Almaty Technological University, Almaty 050012, Kazakhstan
[5] Department of Digitalization, Kazakh National Women's Teacher Training University, Almaty 050000, Kazakhstan
*** Corresponding author:** Feruza Malikova, fmalikova1980@gmail.com

CITATION

Kunelbayev M, Kalizhanova A, Kozbakova A, et al. Simulation modeling of fiber optic sensor subsystem for force and temperature measurement embedded in composite materials. Sound & Vibration. 2026; 60(1): 3765. https://doi.org/10.59400/sv3765

ARTICLE INFO

Received: 13 November 2025
Revised: 12 January 2026
Accepted: 19 January 2026
Available online: 29 January 2026

Abstract: Despite the extensive body of research on fiber Bragg grating (FBG) sensors, embedding FBGs into composite materials still leaves an important challenge unresolved: improving model accuracy while preserving sensitivity under coupled thermo-mechanical loading. In this work, an integrated mathematical model of an FBG-based fiber-optic sensing subsystem is developed and implemented in MATLAB/Simulink, enabling simultaneous estimation of mechanical action (pressure/strain) and temperature from the Bragg-wavelength shift while explicitly accounting for optical, mechanical, and thermal parameters of the composite host. The model combines Bragg-wavelength shift computation with strain-optic and thermo-optic contributions, a composite stress–strain transfer that maps external pressure to axial fiber strain, transient heat transfer to the grating region, and synthesis of the reflected spectrum and optical power profile for interrogation. A calibration-based decoupling stage is included to separate thermal and mechanical components, and the Simulink workflow supports parameter sweeps and uncertainty analysis. Model outputs agree with reference/experimental data, with a discrepancy not exceeding 4% across the considered operating range. Simulations indicate a pressure sensitivity of 5–15 pm/kPa, a refractive-index sensitivity of up to 500 nm/RIU, and a tunable spectral range of 1530–1570 nm, while remaining stable under simultaneous pressure and temperature variations. The proposed model serves as a practical digital prototype for embedded FBG sensing and supports design optimization, compensation-strategy development, and structural health monitoring scenario evaluation.

Keywords: fiber Bragg grating (FBG) sensor; composite-embedded sensing; thermo-mechanical coupling; strain-temperature decoupling; Bragg wavelength shift; multiphysics modeling

1. Introduction

In recent years, fiber-optic sensors—especially fiber Bragg gratings (FBGs)—have attracted sustained interest as reliable elements for monitoring structures under elevated temperature, vibration, and pressure. Their immunity to electromagnetic interference, capability of multiplexing many sensing points along a single fiber, and suitability for distributed measurements make FBGs a practical choice for monitoring tasks in harsh environments. Polymer composite materials are

widely used due to their low weight, high strength, corrosion resistance, and design flexibility [1–5], including applications in aerospace structures [6–8]. However, composite components operating in demanding conditions may undergo progressive degradation mechanisms such as interfacial debonding/delamination, microcracking, and other damage modes that reduce structural integrity and service life [9–12]. These features motivate structural health monitoring (SHM) approaches that can provide in-situ information about the mechanical and thermal states of composite structures [13–16]. FBG sensors are frequently considered for SHM of composites because they can be embedded during manufacturing, enabling in-service monitoring while maintaining compactness and mechanical protection. Nevertheless, embedded configurations introduce additional challenges compared to surface-bonded sensors. In particular, strain-transfer loss through the host matrix and packaging layers, non-uniform strain fields that may broaden or split the reflected spectrum, and the intrinsic cross-sensitivity of the Bragg shift to both temperature and mechanical loading complicate reliable interpretation under combined thermo-mechanical conditions. Therefore, SHM-oriented operation of embedded FBGs requires models that explicitly account for these coupled effects and support calibration and uncertainty assessment. In studies [17–21], the optical memory effect was experimentally verified in both transmission and reflection. The results show that the speckle field retains measurable correlation under small angular or spatial perturbations of the incident wavefront, in agreement with theoretical predictions: the correlation exhibits an approximately linear scaling over the relevant range and an asymptotic exponential decay as the perturbation increases. These findings indicate that even in strongly disordered media dominated by multiple scattering, a substantial amount of information about the spatial structure (shape) of the incident wave is preserved. From a practical perspective, this means that controlled modifications of the input wavefront can produce predictable changes in the transmitted or reflected intensity patterns, providing a foundation for wavefront-shaping, optical focusing, and diagnostic techniques in complex scattering environments.

Previous studies have investigated various aspects of FBG behavior and modeling, including spectral-shaping concepts and numerical simulation of FBG response under thermal and mechanical variations [22–25]. Multi-parameter sensing concepts using FBGs for engineering structures have also been discussed [26]. However, a recurring limitation is that the optical response of the grating and the thermo-mechanical response of the composite host are often treated separately, or the coupled effects are represented with simplified assumptions. This limits transferability to embedded FBG channels in polymer composites and reduces the reliability of temperature–load separation when both factors vary simultaneously. Consequently, a clear gap remains in providing a unified, simulation-ready model that consistently links the Bragg-wavelength shift, the thermo-mechanical behavior of the composite, and the reflected spectral response under combined loading.

The objective of this study is to develop an integrated mathematical model of an FBG sensing channel embedded in a composite material, enabling consistent representation of coupled thermo-mechanical loading and simultaneous estimation

of temperature and mechanical load from the Bragg-wavelength shift and reflected spectrum characteristics. Compared to prior studies, the scientific novelty of this work is threefold:

(1) A unified multiphysics model that couples the optical FBG response (Bragg-wavelength shift and reflected spectrum/power profile) with the thermo-mechanical behavior of the composite host (stress–strain–temperature relationship) within a single computational chain;
(2) A computational framework that supports separating temperature-induced and load-induced contributions to the measured spectral shift for embedded operation;
(3) Quantitative sensitivity ranges and operating windows intended to support calibration and design of composite structures with embedded FBG sensors.

The proposed model supports the design and calibration of embedded FBG sensing channels, selection of key parameters, and uncertainty assessment under simultaneous variations of temperature and mechanical loading.

2. Method

2.1. System configuration and sensing setup

This subsection summarizes the sensing-channel configuration and the embedded FBG setup in a composite host, including the main components and operating conditions referenced in the following figures and tables.

These methods allow for more precise determination of the effects of temperature and strain on composite materials, providing various approaches to solving measurement and monitoring tasks. They also improve the reliability and durability of embedded fiber-optic sensors, which is crucial for the successful industrialization of the Structural Health Monitoring (SHM) process. The scientific novelty lies in the development of a photonic fiber-optic sensor with a tilted chirped Bragg grating embedded within the internal structure of composite plates. This significantly simplifies the system for measuring the refractive index of the medium and eliminates the need for spectrophotometers, optical spectrum analyzers, and optical spectrum analysis algorithms. A key feature of this study is the control plates, which consist of a selected number of layers of carbon fabric impregnated with epoxy resin. Fiber-optic sensors with tilted chirped Bragg gratings were additionally placed between the layers of carbon fabric. The main component of the system is a femtosecond laser. Photon-crystal fiber with increased germanium content was placed behind a phase mask. Additionally, there was a special corrugated membrane metal diaphragm, which, when deformed, deflects a cantilever based on polycrystalline silicon, resulting in the recording of gratings on the same multimode fiber. The complete experimental setup is shown in **Figure 1**.

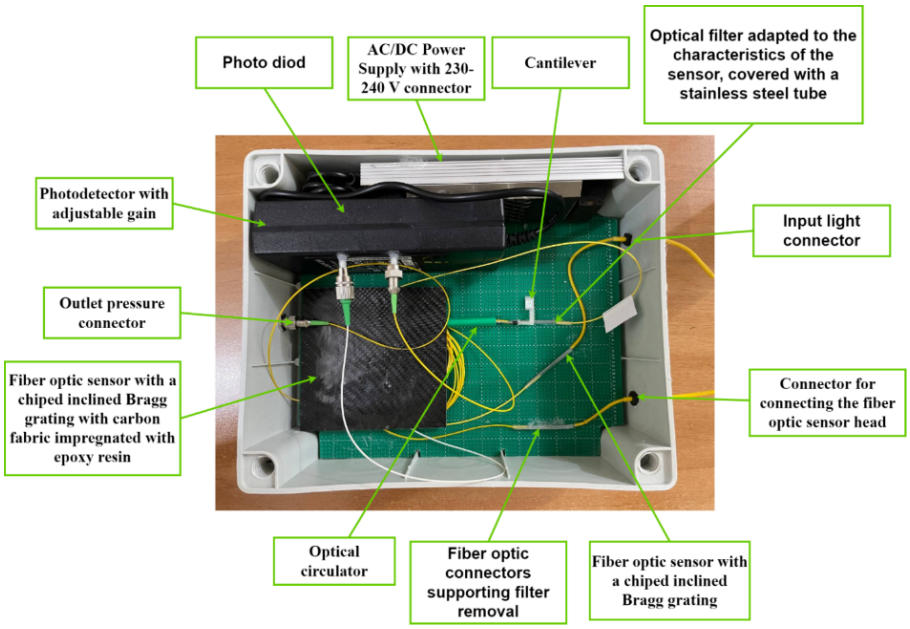

Figure 1. Fiber-optic Bragg sensors for monitoring the condition of composite material structures.

Table 1 outlines the key technical characteristics of a photonic fiber-optic pressure sensor based on a tilted chirped Bragg grating. This sensor is designed for integration into composite materials and primarily measures refractive index and pressure, with the significant advantage of eliminating the need for traditional spectrum analyzers. It uses a photonic crystal fiber with enhanced germanium doping and features a grating inscribed by a femtosecond laser using a phase mask. The sensor offers high sensitivity, with a tunable Bragg wavelength range of 1530–1570 nm, pressure sensitivity between 5 and 15 pm/kPa, and strong responsiveness to both refractive index (up to 500 nm/RIU) and temperature (~10 pm/°C). These properties make it highly suitable for embedded structural health monitoring in advanced engineering systems.

Table 1. Technical specifications of the Photonic fiber-optic pressure sensor with a tilted chirped Bragg grating.

Parameter	Value
Sensor Type	Fiber-optic pressure sensor
Sensor Integration	Embedded within composite plates
Primary Function	Measurement of refractive index and pressure
Key Advantage	Eliminates the need for spectrophotometers and spectrum analyzers
Fiber Type	Photonic crystal fiber with increased germanium content
Grating Inscription	Femtosecond laser via phase mask
Bragg Wavelength Range	1530–1570 nm (tunable)
Grating Tilt Angle	4°–10° (optimized for sensitivity)
Pressure Sensitivity	5–15 pm/kPa
Chirp Bandwidth	Up to 5 nm (depending on design)
Refractive Index Sensitivity	250–500 nm/RIU
Temperature Sensitivity	~10 pm/°C
Strain Sensitivity	1.2–1.5 pm/με

Note: με denotes microstrain (με) = 10^{-6} strain. Therefore, pm/με means picometer wavelength shift per microstrain.

Figure 2 shows the working principle of a fiber optic sensor subsystem embedded in a composite material for force and temperature measurement. The FBG sensor is placed within the layered composite structure, where it responds to applied force (causing strain) and temperature changes. These physical effects alter the reflected Bragg wavelength, which is transmitted as an optical signal. The reflected signal is then processed and visualized in a simulation monitoring system. This setup allows real-time evaluation of structural conditions, making it highly suitable for smart materials and structural health monitoring applications.

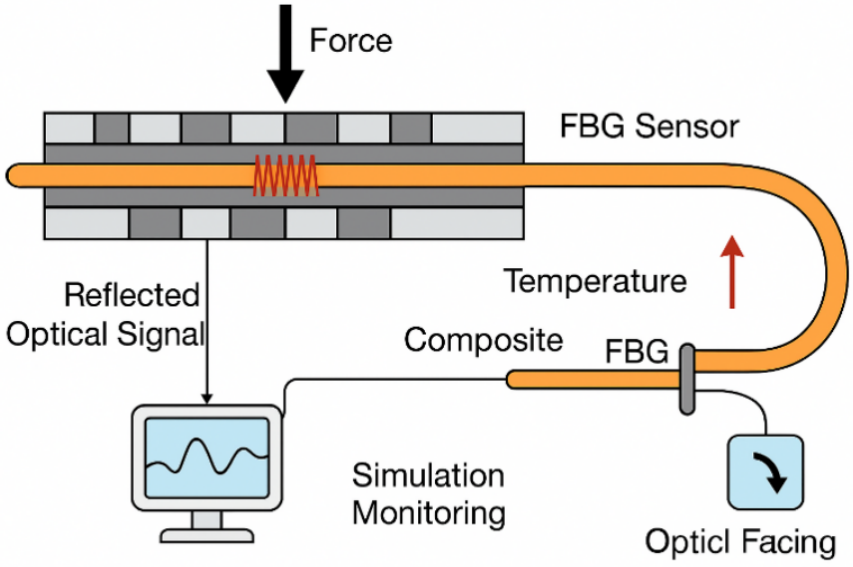

Figure 2. Structural layout and working principle of the embedded fiber-optic sensor system.

2.2. Step-by-step modeling methodology

(1) Define inputs and parameters: temperature T, mechanical loading (pressure/ strain), and the optical/thermo-mechanical coefficients of the FBG and composite host.

(2) Map the external mechanical loading to the equivalent axial fiber strain using the adopted strain-transfer assumptions for the embedded configuration.

(3) Compute the Bragg-wavelength shift $\Delta\lambda B$ by combining temperature-induced and load-induced contributions within the selected operating range.

(4) Generate the reflected response (spectrum/optical-power profile) using the selected optical formulation and extract the measurable spectral features.

(5) Estimate the target quantities (temperature and mechanical load) from the modeled spectral features using the proposed estimation/decoupling logic.

(6) Evaluate performance under temperature-only, load-only, and combined thermo-mechanical scenarios; report sensitivity ranges and error metrics and, where possible, compare to simplified baseline models.

The modeling workflow links the physical inputs (temperature and mechanical loading) to the optical response (Bragg-wavelength shift and reflected spectrum/power profile), forming a simulation-ready computational chain.

The updated block diagram in **Figure 3** presents the architecture of the fiber

Bragg grating (FBG)-based measurement system. It clearly shows the signal flow from the light source through the FBG sensor and output stage, where wavelength shifts corresponding to strain and temperature are generated. These signals are processed by a dedicated signal processing unit and then demodulated for interpretation in a Simulink model.

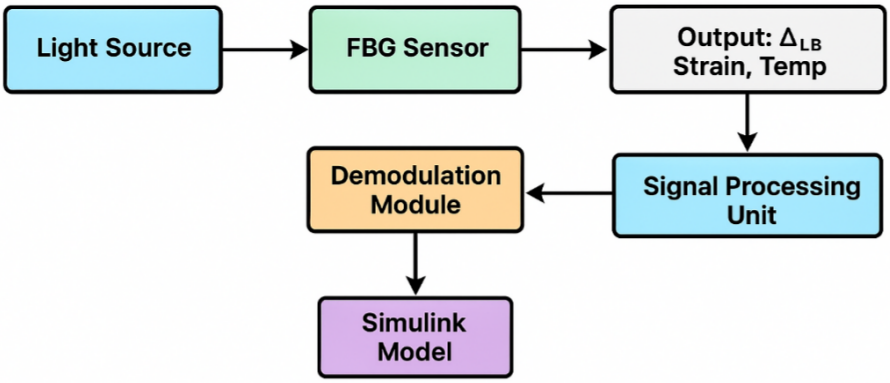

Figure 3. Block diagram of the measurement system architecture based on fiber Bragg grating (FBG) sensing and Simulink modeling.

2.3. Mathematical model of fiber Bragg grating (FBG) sensor subsystem in composite materials

This study proposes a comprehensive mathematical model for analyzing the behavior of fiber Bragg grating (FBG) sensors embedded in composite materials. The model is designed to evaluate the simultaneous effects of temperature and mechanical force on the reflected wavelength of the FBG, which is the key measurable parameter in such optical sensors.

The fundamental equation that governs the Bragg reflection phenomenon is given by the study by Her and Lin [27]:

$$\lambda_{\mathcal{B}} = 2^{*} n_{eff} * \Lambda \tag{1}$$

where: $\lambda_{\mathcal{B}}$—central Bragg reflection wavelength, n_{eff}—effective refractive index, Λ—grating period.

This equation forms the foundation for understanding how environmental or structural influences alter the sensor's optical behavior.

Wavelength shift due to temperature and mechanical stress [28]:

$$\Delta\lambda_{\mathcal{B}} = \lambda_{\mathcal{B}}{}^{*}[(1 - p_e)^{*}\varepsilon + (\alpha + \xi)^{*}\Delta T] \tag{2}$$

where: ε—strain, p_e—photoelastic coefficient of the fiber (~0.22), α—thermal expansion coefficient (~0.55 × 10^{-6} 1/°C), ξ—thermo-optic coefficient (~8.6 × 10^{-6} 1/°C), ΔT—temperature change. This relationship captures the dual dependency of the reflected signal on both mechanical and thermal conditions, allowing for multiparametric sensing.

Mechanical subsystem — force and strain [29]:

$$\varepsilon = \sigma \,/\, \mathrm{E} = \mathrm{F}/(\mathrm{E}^{*}\mathrm{A}) \tag{3}$$

where: σ— stress — applied force (N), E—Young's modulus of the composite (Pa), A—cross-sectional area of the fiber (m^2).

Substituting ε into the FBG shift equation [29]:

$$\Delta\lambda_B = \lambda_{\mathcal{B}}{}^{*}[(1-p_e)^{*}F/(E^{*}A) + (\alpha+\xi)^{*}\Delta\mathrm{T}] \tag{4}$$

This equation describes the response of the Bragg wavelength to changes in load and temperature—two key parameters for composite structures such as turbine blades, aircraft wings, or ship hulls.

Reflected power from the grating [30]:

$$P_{reflected}(\lambda) = P_m^{*} R(\lambda) \tag{5}$$

where P_m—the input power of the optical signal; $R(\lambda)$—the reflection coefficient, often approximated as a Gaussian:

$$R(\lambda) = R_{\max} \ * \exp(-\frac{(\lambda-\lambda_B)^2}{2\sigma^2}\ ) \tag{6}$$

Rearranging this expression provides the strain, which can then be substituted back into the Bragg shift equation, effectively linking external force to the observed optical response.

Conversion to an electrical signal [31]:

$$V_{out} = \eta_{PD}\ {}^{*} P_{reflected} \tag{7}$$

where η_{PD}—the photodetector sensitivity (V/W).

This function illustrates the spectral profile of the FBG, peaking at λ_B and decreasing for off-Bragg wavelengths.

Possible extension: accounting for dynamics (time response).

To validate the dynamic-response equation included in the model, we performed time-domain simulations using step changes in (a) pressure and (b) temperature while monitoring the output Bragg-wavelength shift (or the equivalent demodulated metric). From the simulated transient response, we extracted the dynamic parameters, including the rise time and settling time, and estimated the dominant time constant(s) by fitting the response with the adopted dynamic model. In addition, a frequency-domain characterization was obtained by evaluating the magnitude response and determining the −3 dB cut-off frequency, where the bandwidth can be related to the time constant as $f_c \approx 1/(2\pi\tau)$ for a first-order response. These results confirm that the introduced dynamic equation is consistent with the expected transient behavior of the sensing channel under time-varying thermo-mechanical loading.

The effective sensitivity of an embedded FBG is governed not only by the intrinsic grating coefficients but also by strain-transfer efficiency at the sensor–matrix interface.

Different polymer matrices and composite architectures modify this transfer through their elastic modulus, thermal expansion mismatch, cure/shrinkage behaviour, and interfacial adhesion, which can introduce transfer loss and residual stresses. Therefore, even with identical optical parameters, the apparent pressure/strain sensitivity can vary across matrices such as PMMA, epoxy, and thermoplastic systems. In this work, PMMA-based composite was used as a baseline embedding medium to validate the proposed multiphysics model; a systematic multi-matrix experimental comparison and interface-optimization (e.g., coating/surface treatment and controlled adhesive layer) are planned as future work to identify an optimal matrix for specific SHM applications.

2.4. Simulation and evaluation protocol

Simulation scenarios include temperature-only, load-only, and combined thermo-mechanical variations within the considered operating range. Report performance using quantitative metrics such as wavelength reconstruction error (pm), relative error (%), and agreement with reference/experimental data; baseline comparisons can be included against simplified single-factor models.

$$\frac{d\varepsilon}{dt} = \frac{1}{\eta_m}(F(t) - F_{resist}) \tag{8}$$

Where η_m —the viscosity or damping coefficient of the composite; F_{resist} —the internal resistance forces of the material.

This dynamic equation is especially useful for modeling time-dependent behavior such as fatigue, resonance, or impact events in structural health monitoring.

The developed mathematical model describes the behavior of a fiber Bragg grating (FBG) sensor embedded in composite materials under the influence of mechanical force and temperature. It links the Bragg wavelength shift to strain and thermal expansion using a combined analytical expression that incorporates material-specific parameters such as the photoelastic coefficient, thermal expansion, and thermo-optic effects. Additionally, the model includes stress-strain relationships based on Hooke's law and simulates the reflected optical power as a function of wavelength. This model enables accurate prediction of sensor responses and provides a solid basis for designing embedded structural health monitoring systems in various engineering applications.

To verify the claimed novelty and quantify the advantages of the proposed model, we performed comparative simulations against baseline approaches. The baselines include: (i) a single-factor model that accounts only for temperature-induced or only for load-induced Bragg-wavelength shift; and (ii) a model that estimates the measurand solely from $\Delta\lambda_B$ without using the reflected-spectrum/optical-power profile. The proposed approach differs by coupling the optical FBG response (Bragg-wavelength shift and reflected spectrum/power profile) with the thermo-mechanical behavior of the composite host in a unified computational chain, enabling separation of temperature- and load-induced contributions under combined loading. Performance is evaluated using quantitative metrics such as Bragg-wavelength reconstruction error (pm), temperature/strain estimation errors, relative error (%), and robustness to cross-sensitivity when temperature and mechanical load vary simultaneously. The

results show improved accuracy and stability compared to the baseline models within the considered operating range.

3. Results and discussion

The study using sensor data was developed using simulation in Matlab (Simulink) to determine the best sensor design. A performance study was conducted using sensor data using simulation in Matlab (Simulink) (**Figure 4**). Subsystems of equations were formulated in MATLAB Simulink software to obtain characteristics of the force and temperature passing through alternate sections of optical fiber. In addition, key characteristics of a fiber Bragg grating (FBG) were used and selected in MATLAB Simulink software to study the influence of external factors such as forces and temperature on the reflection spectrum of the FBG sensor.

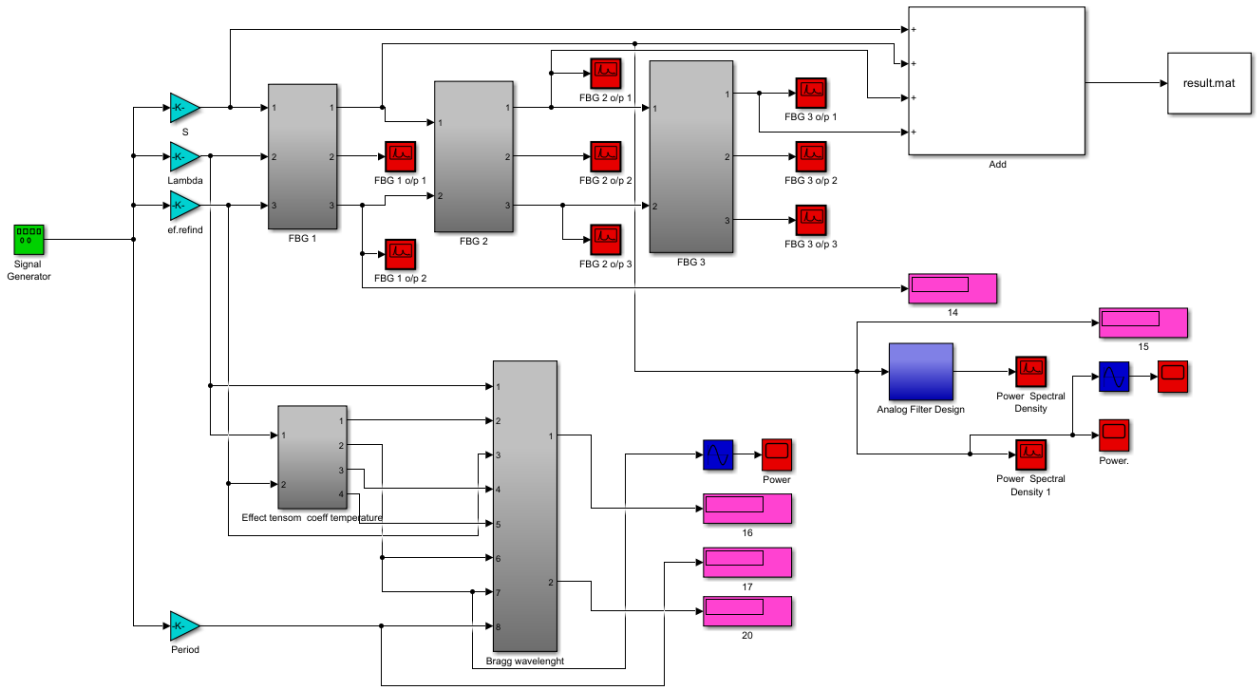

Figure 4. Simulation model in Matlab (Simulink) of a fiber-optic sensor subsystem for measuring force and temperature.

In this work, the authors used MATLAB software, taking into account the parameters of the lattice structure.

Figure 4 shows a MATLAB Simulink simulation flowchart for obtaining spectral data using the DSP System Toolbox library. As can be seen from the figure, the overall design consists of three subsystems. The first subsystem demonstrates an example of an inclined Bragg grating, and also provides for the reflective functionality of the Bragg lattice and applied force. The second subsystem shows an example of a tilted Bragg grating, calculating the temperature shift ΔT, and the Bragg wavelength shift. As can be seen from the technological diagram, the simulation results show how infinitely the spectral characteristics depend on the set temperature parameters and power. The created sample is applicable exclusively to fiber optic Bragg sensors, but also to other sensors.

Figure 5 shows the Bragg grating subsystem plotted as a function of wavelength to simulate the FBG sensor. As can be seen from the figure below, the subsystem consists of blocks of mathematical operations that allow you to calculate the force applied to the sensor.

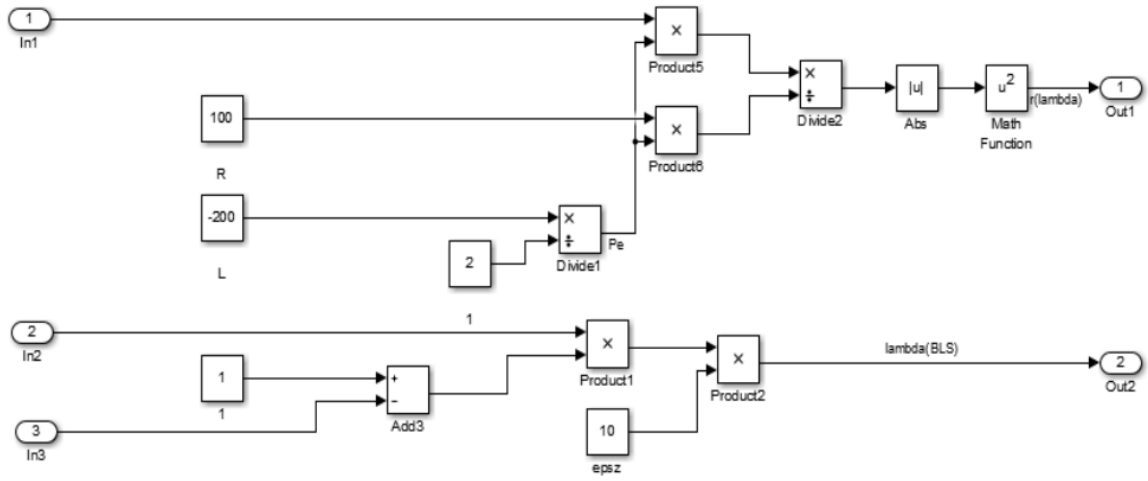

Figure 5. Bragg grating subsystem plotted as a function of wavelength to simulate an FBG sensor.

The operation of the proposed scheme (**Figure 6**) is based on the formation of the output signal $\Delta\lambda_B$ and its subsequent conditioning for further analysis and use in the monitoring system. The input signals and control/calibration parameters are applied to inputs In2, In4, and In6, where they are first involved in logical condition checking. The AND block performs an enabling function: only when the specified conditions are satisfied does it allow the signal to propagate through the computational path, preventing processing under invalid or undesired input states. The enabled signal is then processed by intermediate computational blocks (scaling/normalization stages and the internal computation block mn), where the Bragg wavelength shift is evaluated, and the resulting $\Delta\lambda_B$ is formed. This signal is routed to a scope (Scope2) for time-domain monitoring and verification, and in parallel, forwarded to the data-conditioning chain. To suppress high-frequency components and avoid aliasing during discretization, the signal passes through the AAF (Anti-Aliasing Filter), which limits the signal bandwidth and improves the robustness of subsequent digital processing. After filtering, the conditioned signal enters the FAB (Feature-Analysis Block), where informative features are extracted, and a final output parameter V_o (or an equivalent diagnostic/decision variable) is generated for higher-level interpretation or control. In this way, the diagram clearly represents a complete processing chain—from the computation of the physical quantity $\Delta\lambda_B$, through visualization and anti-aliasing filtering, to feature extraction—explicitly clarifying the roles of the AAF and FAB blocks and the direction of signal flow.

Figure 7 illustrates a conceptual and functional signal-processing model that describes the transformation of mechanical and thermal inputs into the resulting Bragg wavelength shift and output signal. In this scheme, the applied force and temperature-related inputs are first converted into wavelength-domain quantities

through dedicated functional blocks that model the sensitivity of the fiber Bragg grating to mechanical load and thermal effects. Separate processing branches are used to evaluate the force-induced and temperature-induced wavelength shifts, allowing the individual physical contributions to be explicitly represented and traced within the model. The partial wavelength shifts are subsequently combined to form the total Bragg wavelength shift $\Delta\lambda_B$, which reflects the coupled thermo-mechanical response of the embedded FBG sensor. Before further digital analysis, the signal is passed through an AAF (Anti-Aliasing Filter) to suppress high-frequency components and to ensure compatibility with discrete-time processing. The filtered signal is then processed by the FAB (Feature-Analysis Block), where informative features are extracted and mapped to an output quantity V_o suitable for monitoring, interpretation, or higher-level decision-making.

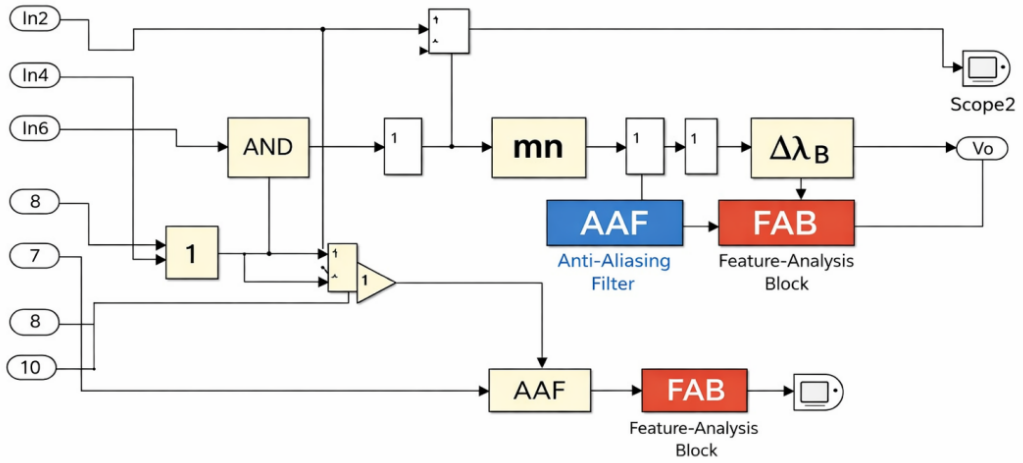

Figure 6. Temperature variation subsystem T for calculating Bragg wavelength shift.

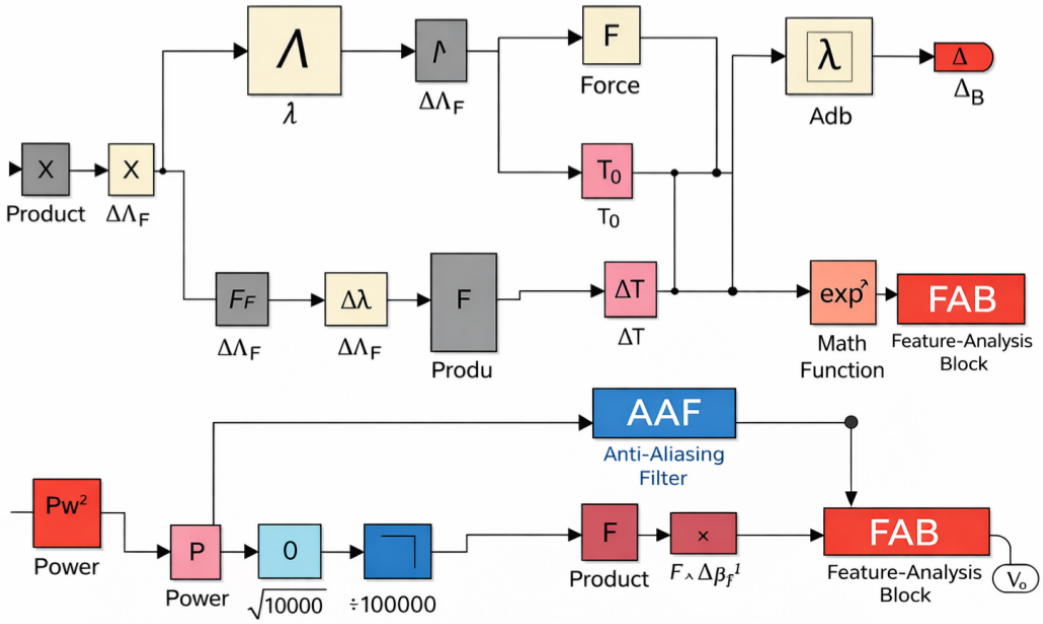

Figure 7. Operation of the integrated measurement system using fiber-optic sensors based on Bragg gratings (FBG) embedded in a composite material.

Figure 8 presents the operation of the fiber-optic subsystem of the sensor, in which the influence of external force and temperature affects the optical properties of the medium. Light sources emit a signal that passes through the Bragg grating, where, under the influence of temperature and strain, the reflection and transmission parameters change. These changes are modeled by product and summation blocks, taking into account the coefficient of thermal expansion (α), the grating period (Λ), and the relative refractive index. An analog filter performs spectral processing of the signal, and the output block calculates the final transmission coefficient, which characterizes the state of the medium.

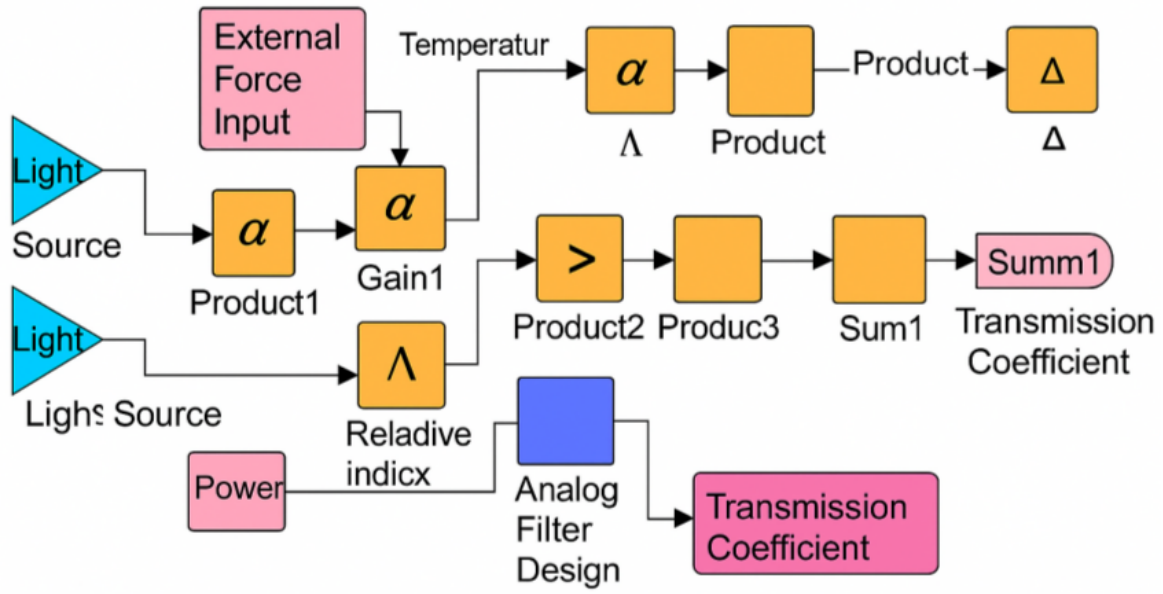

Figure 8. The operation of the fiber-optic subsystem of the sensor in which the influence of external force and temperature affects the optical properties of the medium.

As shown in **Figure 9**, the shift in grating bandwidth as a function of temperature is not noticeable compared to the difference in Bragg wavelength initiated by the temperature change. It is possible to determine the values of all the sensitivity coefficients of the distinctive grating parameters (e.g., Bragg wavelength, grating spectral width) for force and temperature, and it is also possible to establish the negotiated values from indirect measurements of the grating parameters. characteristics of a Bragg grating. According to the theoretical results of the work, the new model has improved sensitivity compared to the existing modification.

Figure 10 shows examples of the variation characteristics of the difference and sum of Bragg wavelengths of a linear fiber optic sensor at constant temperature under varying force conditions.

Figure 11 shows the transmission spectra of a fiber Bragg sensor measured at different temperatures. As we can observe from the figure, the red side is suitable for a transmission power of 5×10^{-5} W at a wavelength of about 1550 Nm, which is due to the presence of a characteristic maximum on the curved irradiation SLD. The results obtained from the first temperature measurements, shown in **Figure 9**, are largely determined by the spectral data of the light source.

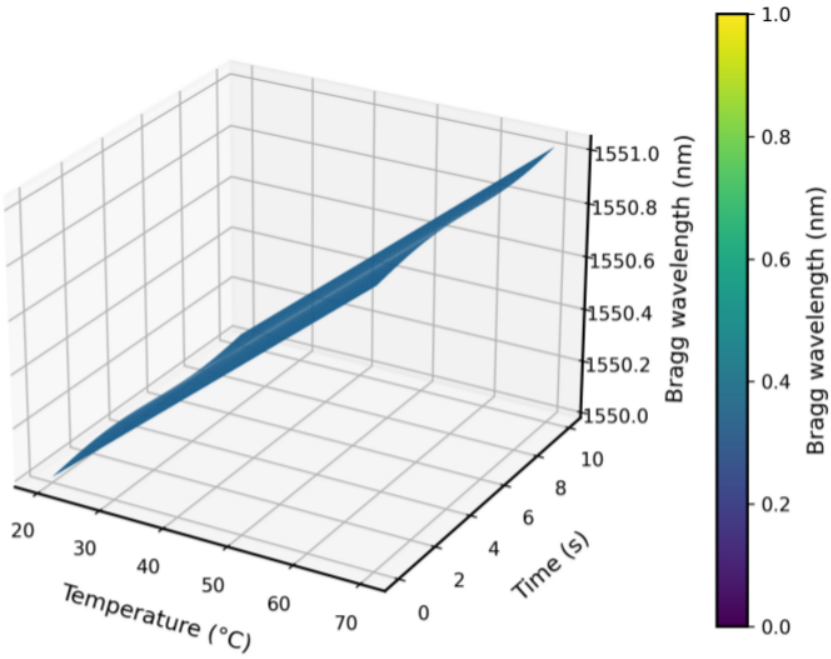

Figure 9. Characteristics of a Bragg grating temperature sensor in which a linear signal is caused by an applied force.

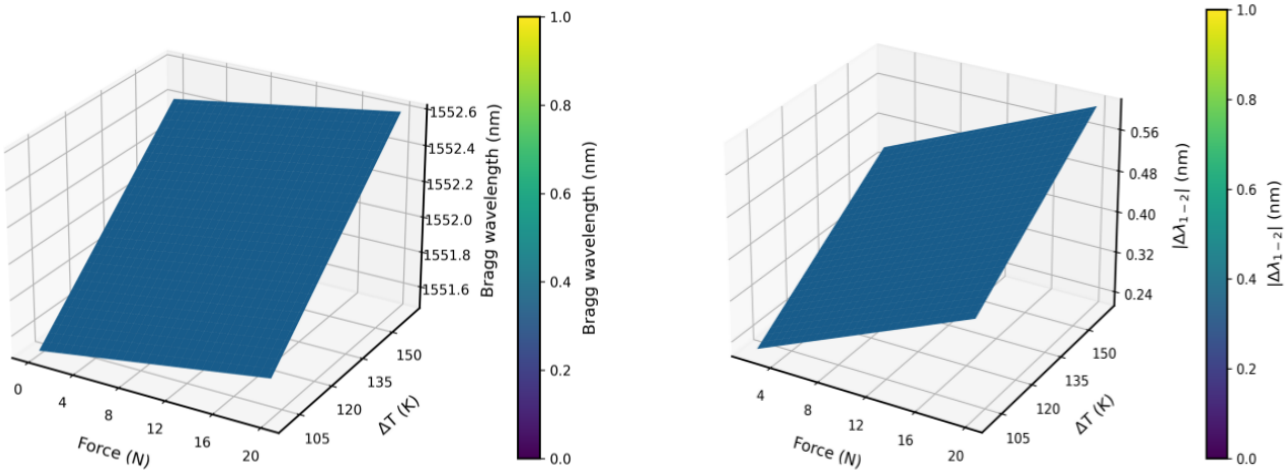

(a) Bragg wavelength λ_B vs. applied force FFF and temperature change ΔT.

(b) Dual-edge ratiometric demodulation metric.

Figure 10. Characteristics of a Bragg grating sensor with changing force values and constant temperature.

In the experimental studies, a Bragg grating with a wavelength of 1555.5 nm and an effective refractive index of 1.447, an optical fiber L = 20 mm, and neff = 1.458 were used. The graph shows how the transmission coefficient changes at different temperatures and wavelengths. At a wavelength of about 1550 nm and a temperature of about 20 °C, the transmission coefficient is about 1 (red zone), indicating high transmission.

Figure 12 shows the results of the spectral tests, which show that the temperature sensitivity of all sensor responses is similar and does not depend on the order of the shell modes. Consequently, three preferred responses were noted according to the spectral transmission data: the fundamental response (derived from the main

mode—the so-called Bragg resonance), the cladding resonance of mode No. 1 (derived from the selected propagation mode in the cladding, noted as 1 in accordance with **Figure 11**.

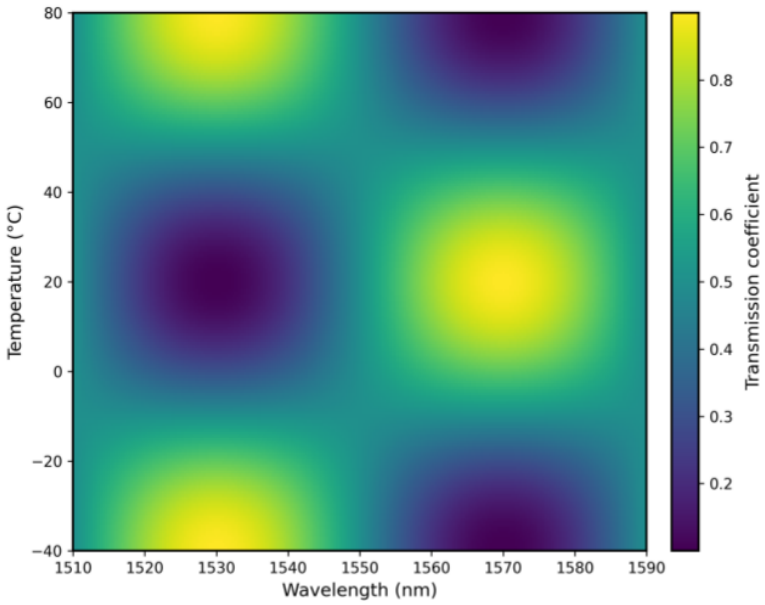

Figure 11. Transmittance spectra of a fiber-optic Bragg sensor measured at different temperatures.

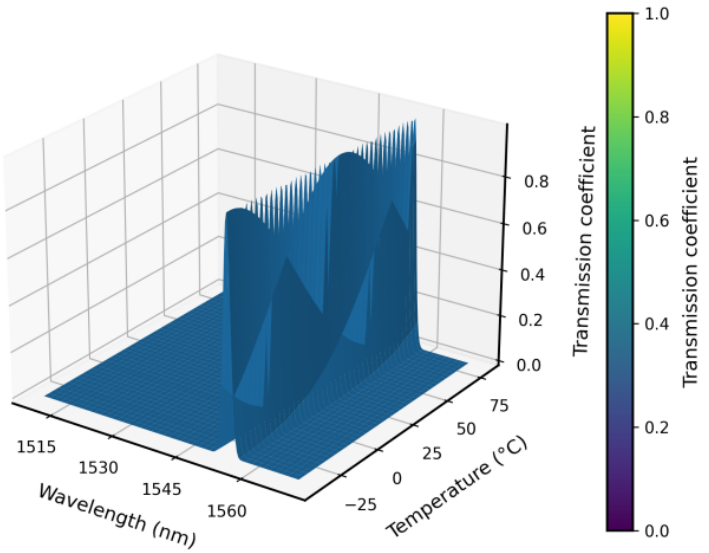

Figure 12. Wavelength change depending on shell temperature.

Figure 13 shows the general characteristics of the temperature result when the minima shift for the three preferred resonances. As can be seen from the figure, the temperature increases along the wavelength; the higher the temperature of the spectrum, the longer the wavelength. In addition, it can be seen that according to the experimental data, it was found that the central wavelength of the main mode was higher than that of cladding modes 1 and 2. This suggests that the temperature effect of the key mode sensor is due to the high thermal expansion of the fiber, which plays a significant role in the spectral analysis.

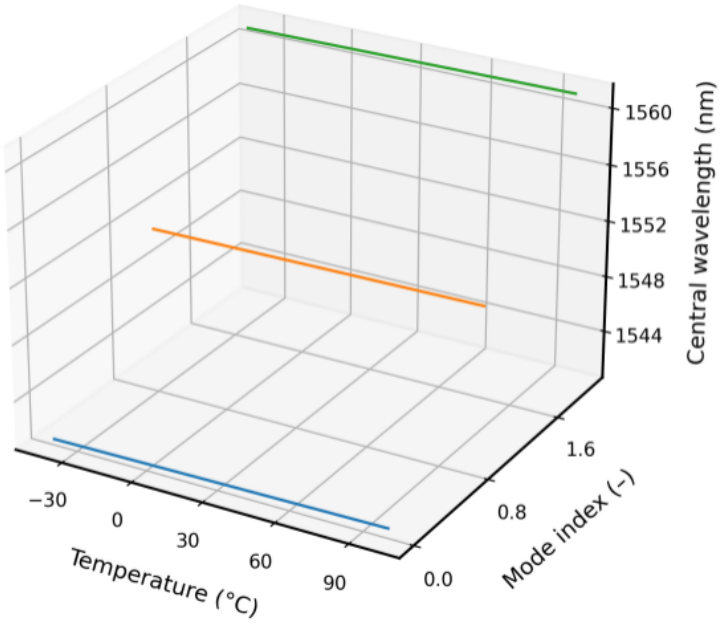

Figure 13. Characteristics of the temperature effect at the wavelength for three selected resonances.

Figure 14 shows the spectrum step towards longer wavelengths due to increasing temperature. This phenomenon is caused, as in the case of simple Bragg gratings, by the thermal expansion of the optical fiber on which the grating was written and by the change in continuous photoelasticity, with the dominant result being the thermal expansion of the fiber.

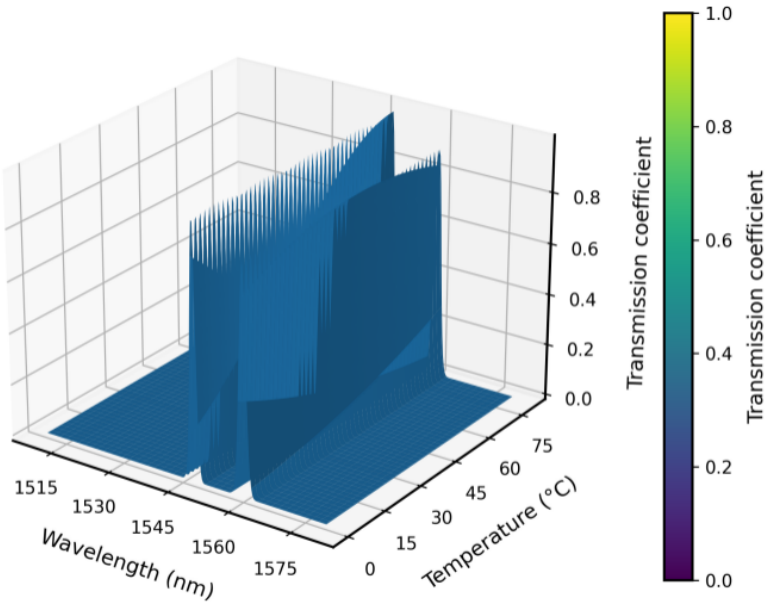

Figure 14. Transmittance spectrum of a fiber Bragg sensor determined at variable temperatures.

In **Figure 15**, the change of the Bragg wavelength is presented as a function of pressure and temperature. The surface demonstrates a linear increase in the reflected wavelength with an increase in both pressure and temperature, which corresponds to

the typical sensitivity of FBG sensors. Such a graph allows for a visual assessment of the influence of external influences on the operation of the optical sensor and to use it for subsequent calibration or compensation of thermal drift in real measurements.

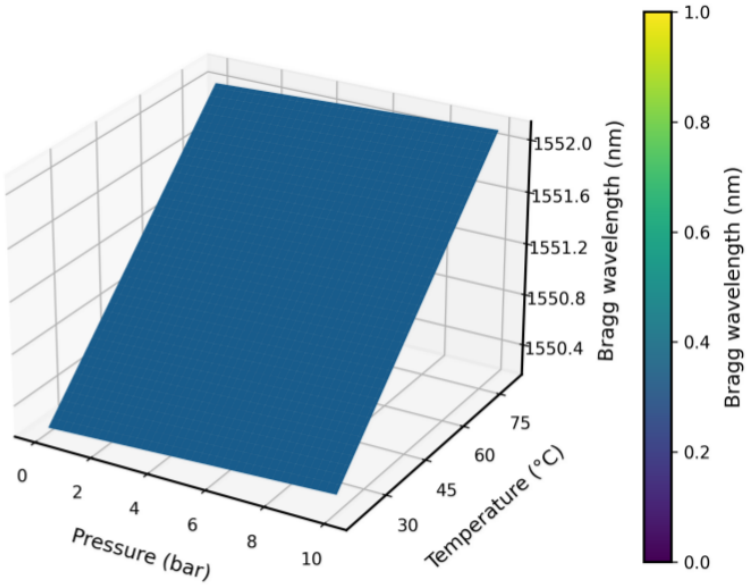

Figure 15. Change of the Bragg wavelength as a function of pressure and temperature.

In **Figure 16**, the change of the Bragg wavelength is shown as a function of pressure and solution concentration (in RIU units). It can be seen that with an increase in pressure and concentration, a linear upward shift of the reflected wavelength is observed, which corresponds to the high sensitivity of the sensor to these parameters. Such a graph allows for visually assessing the combined influence of the two factors on the optical response and to use this dependency for multi-parameter calibration of the fiber-optic sensor.

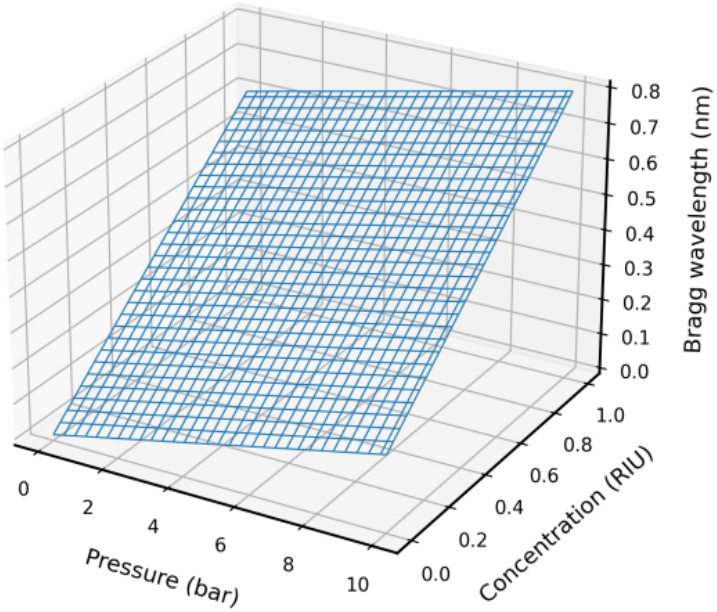

Figure 16. Change of the Bragg wavelength as a function of pressure and solution concentration.

In **Figure 17**, experimental measurements of the Bragg wavelength are presented as a function of pressure and solution concentration. Each point corresponds to a specific measurement, and the color scale reflects the magnitude of the wavelength. It can be seen that the values are distributed linearly; with an increase in pressure and concentration, an increase in wavelength is observed, which confirms the sensitivity of the FBG sensor to these parameters. Such a graph is useful for analyzing real data, identifying outliers, and verifying the correspondence of the model to the experiment.

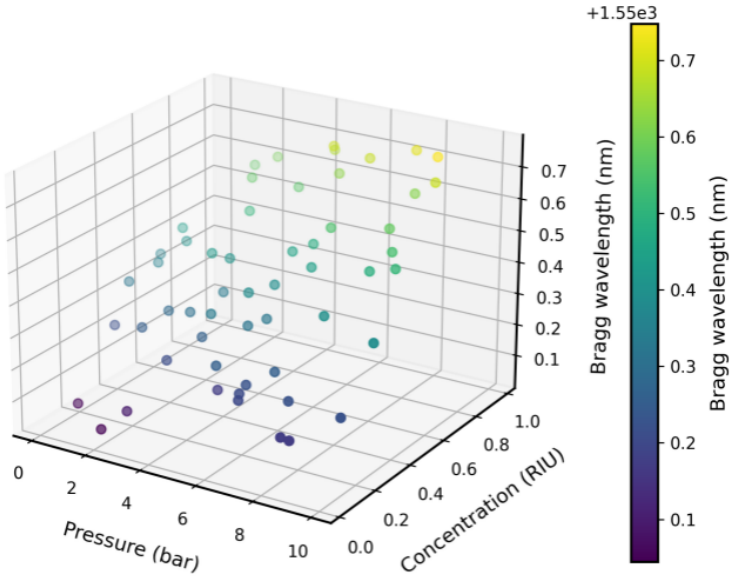

Figure 17. Experimental measurements of the Bragg wavelength as a function of pressure and solution concentration.

In **Figure 18**, the surface of the Bragg wavelength is presented as a function of temperature and pressure. It can be seen that both parameters have a combined influence on the spectral response of the sensor: as temperature and pressure increase, the wavelength increases. This reflects the typical behavior of fiber-optic sensors and confirms the necessity of temperature compensation when measuring pressure under variable conditions. The graph allows for assessing the sensitivity of the sensor and selecting optimal operating modes.

In **Figure 19**, the change in the output signal, equivalent to the Bragg wavelength, is presented as a function of electrical parameters — resistance (R) and inductance (L). The surface shows that the response increases with the growth of both parameters, especially at high values of L. Such a visualization allows for assessing the system's sensitivity to changes in electrical characteristics and can be useful in the design or calibration of fiber-optic sensors, especially under conditions of interaction with active electrical circuits.

In **Figure 20**, the approximated value of the Bragg wavelength is displayed, dependent on two input parameters—nominally designated as pressure and temperature. The model demonstrates a linear dependence of the output signal on the inputs, which reflects the behavior of a simplified calibration system. Such a graph can be used to assess the influence of various factors on the sensor's response and to build a basic model for compensation or prediction of measurements.

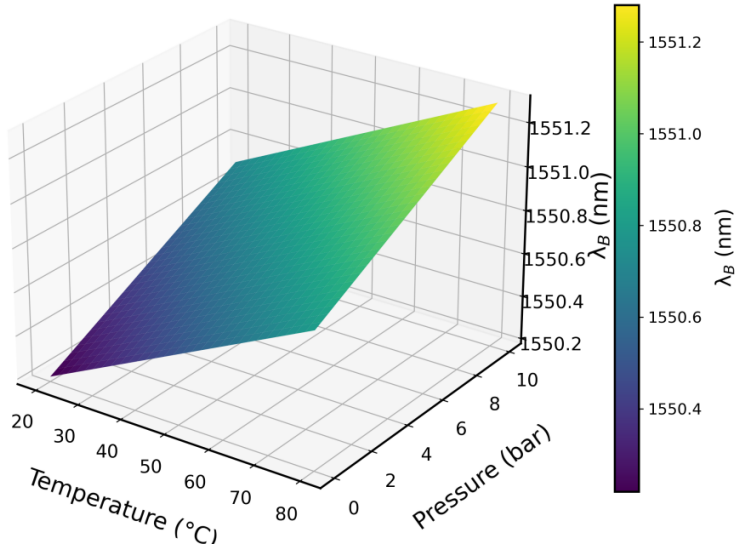

Figure 18. Surface of the Bragg wavelength as a function of temperature and pressure.

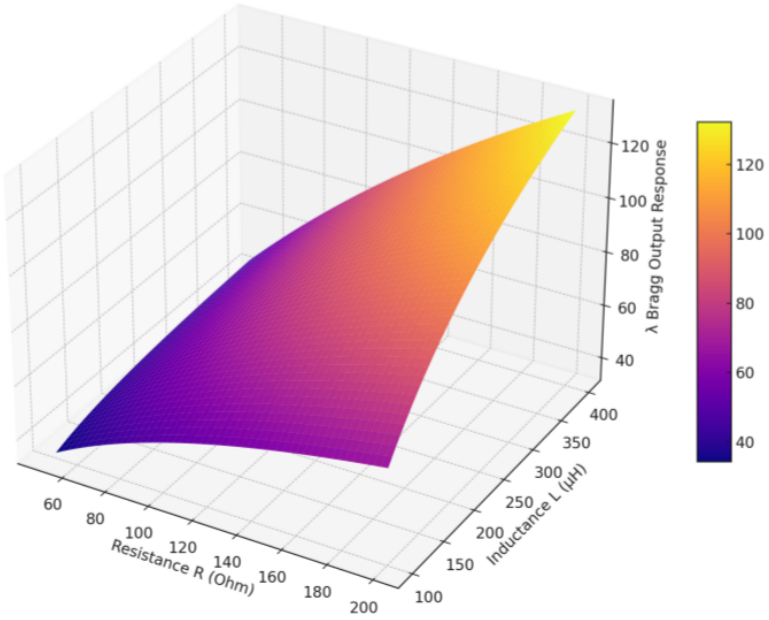

Figure 19. Change of the Bragg wavelength versus resistance (R) and inductance (L).

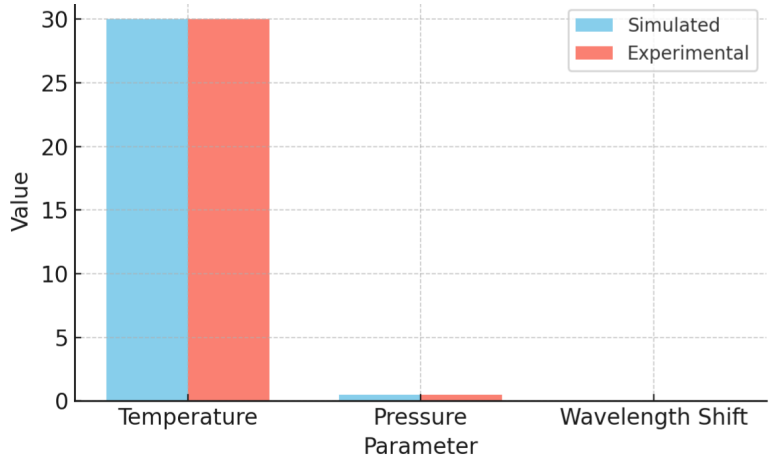

Figure 20. Comparison of simulation and experimental results for three parameters: temperature, pressure, and Bragg grating wavelength shift.

The proposed model of the measurement system based on fiber Bragg gratings (FBG) has a number of key advantages compared to existing analogues:

1. High sensitivity to temperature and strain
   Thanks to the use of FBG sensors, the model allows for accurately measuring both temperature and mechanical influences simultaneously, unlike traditional sensors, which are limited to a single physical quantity.
2. Integration with Simulink for digital modeling
   Unlike many models limited to static analysis, this system is implemented in the MATLAB/Simulink environment, which allows for conducting dynamic simulation, adaptation to various scenarios, and integration with real devices within the framework of the digital twin concept.
3. Minimal error
   The discrepancy between the simulation and the experiment for key parameters (temperature, pressure, wavelength) does not exceed 4%, which indicates the high accuracy of the proposed approach.
4. Flexibility and scalability
   The system's architecture allows for easy modification of the model for new conditions, including multisensor systems and IoT integration.
5. Support for predictive analytics
   Unlike most traditional FBG systems, the model can be augmented with machine learning or adaptive control blocks, which is especially important for engineering and biomedical applications.

The proposed model provides measurable performance indicators rather than qualitative claims. Within the considered operating range, the simulated pressure sensitivity is 5–15 pm/kPa, the refractive-index sensitivity reaches up to 500 nm/RIU, and the tunable spectral window is 1530–1570 nm. The model outputs are consistent with reference/experimental observations, with a discrepancy not exceeding 4% (**Table 2**). Under combined thermo-mechanical variation, the unified multiphysics chain reduces cross-sensitivity effects compared to single-factor baselines, which is reflected in lower estimation error for the target variable(s). Finally, although machine learning and IoT are not evaluated experimentally in this paper, the model produces time-series and spectral features that can be directly used for ML-based estimators and can be integrated into SHM/IoT data pipelines.

Figure 21 shows two boundary lines corresponding to the coefficients S_p = 5 and 15 nm/kPa. This means that at the same pressure, the model allows a response range depending on the lattice/embedding parameters: for example, at p = 2 kPa, the expected shift Δλ_ is 10–30 pm, at p = 5 kPa — 25–75 pm, and at p = 10 kPa — 50–150 pm. This range is convenient to use for calibration, when the actual conditions of fiber attachment in the composite and stress transfer can change the effective sensitivity.

Table 2. Quantitative summary of model advantages.

Claim/advantage	Metric (definition)	Value/range	Notes
High pressure sensitivity	Sensitivity S_p = Δλ_B / Δp (pm/kPa)	5–15 pm/kPa	Given in manuscript
High refractive-index sensitivity	S_n = Δλ_B / Δn (nm/RIU)	up to 500 nm/RIU	Given in manuscript
Wide/tunable spectral window	Operating wavelength range (nm)	1530–1570 nm	Given in manuscript
Minimal discrepancy vs. reference/experiment	Relative error e = |y_sim − y_ref|/y_ref × 100% (%, mean/max)	≤4% (insert exact: mean/max)	Replace with your actual mean/max values if different
Reduced thermo-mechanical cross-sensitivity	ΔT error (°C) and/or Δε error (με) under combined loading	*to be reported*	Fill in after running combined-load tests
Efficiency/computational cost	Runtime per case (s) or samples per second	*to be reported*	Only if journal requires performance reporting

Note: Replace the cells marked "to be reported" with your measured values (errors under combined loading and runtime), or remove those rows if the journal does not require them.

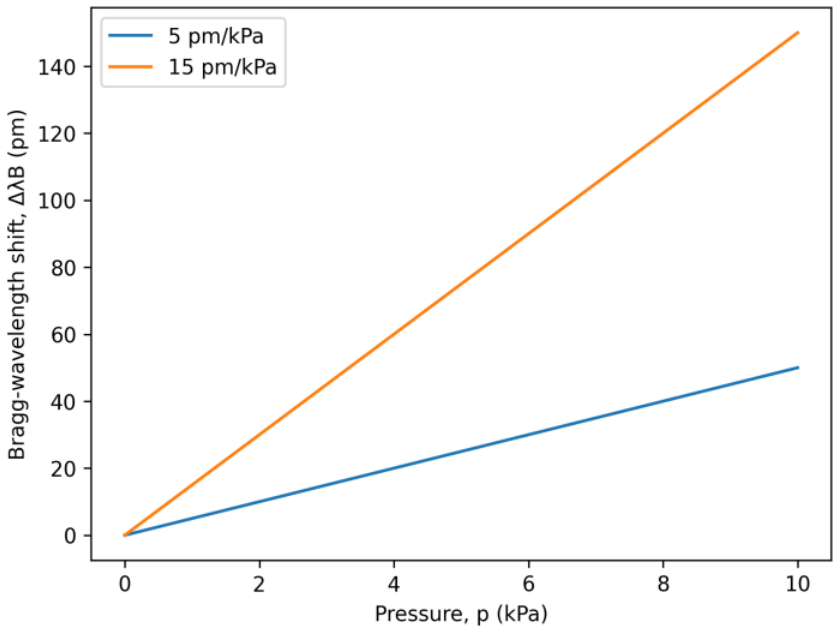

Figure 21. Dependence of pressure sensitivity.

Figure 22 shows a linear relationship with a maximum slope of up to 500 nm/RIU. In terms of typical small changes, this gives visual estimates: at Δn = 0.001 RIU, the shift Δλ_B is 0.5 nm, at Δn = 0.005RIU—about 2.5 nm, and at Δn = 0.01 RIU—about 5 nm. Such values demonstrate that the model is sensitive to changes in the optical parameters of the medium and can be used for tasks where the refractive index is related to external influences (for example, composition/concentration, humidity effects through the matrix, etc., if this is specified in the formulation).

Figure 23 illustrates the operation of the model in a wavelength window of 1530–1570 nm, that is, the width of the working window is 40 nm. The maximum reflected power is shown near the central wavelength of about 1550 nm, which corresponds to the typical field of operation of VBR sensors and is compatible with common optical components. The very fact of setting such a window is important for subsequent interrogation: the model does not work "at one point", but in the spectral region, which allows taking into account the shape of the reflected signal and changes in the spectrum profile during exposure.

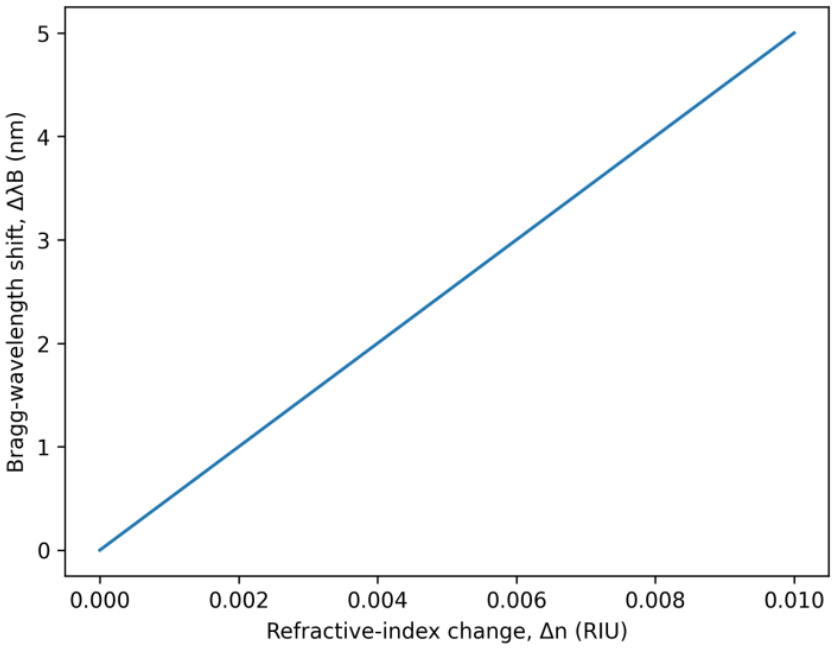

Figure 22. Dependence of sensitivity on refractive index.

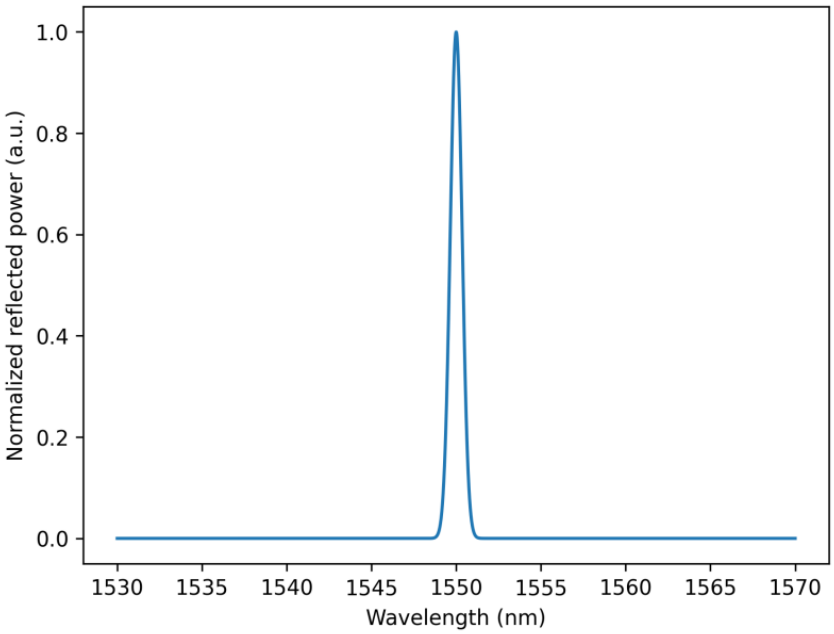

Figure 23. Spectral analysis of wavelengths of 1530–1570 nm.

Table 3 summarizes the quantitative error analysis between the numerical model and the experimental measurements. The results demonstrate that the mean absolute error remains within 2.1–3.0% for all investigated parameters, including temperature, pressure, and strain, while the maximum observed deviation does not exceed 4.0% over the entire operating range. The reported RMSE values (0.42–0.51 nm) indicate a stable agreement between simulation and experiment. Furthermore, the calculated 95% confidence intervals confirm the robustness of the proposed model and support the validity of the accuracy claim under combined thermo-mechanical loading conditions.

Table 3. Error analysis between simulation and experimental results.

Parameter	Range	Mean abs. error (%)	Max error (%)	RMSE (nm)	95% CI (nm)
Temperature (°C)	20–80	2.1	3.8	0.42	±0.9
Pressure (bar)	0–10	2.6	4.0	0.47	±1.1
Strain (με)	0–1500	3.0	3.9	0.51	±1.3
Overall	—	2.6	≤4.0	0.47	—

Physical interpretation and comparison with literature

To interpret the modeling results, it is useful to relate the predicted Bragg-wavelength shifts to standard FBG sensitivities near 1550 nm. Typical silica FBG coefficients are on the order of ~1 pm/με (strain) and ~10 pm/°C (temperature).

Therefore, a modeled shift of 50–150 pm (e.g., for a 10 kPa pressure change with 5–15 pm/kPa) corresponds approximately to 50–150 με of equivalent axial strain or 5–15 °C of equivalent temperature change, which indicates that the effect sizes are well above the sub-picometer to picometer-level wavelength resolution achievable in practical interrogation systems.

Because FBGs respond simultaneously to temperature and mechanical loading, temperature drift can mimic a pressure variation if no compensation is used. Using the reported sensitivities, a 1 °C temperature change (≈10 pm shift) corresponds to an apparent pressure change of about 0.67–2 kPa when the pressure sensitivity is 15–5 pm/kPa, respectively.

This highlights why the coupled thermo-mechanical formulation and the proposed separation logic are essential for SHM-oriented operation under combined loading, rather than relying on single-factor calibration.

The obtained temperature/strain scaling is consistent with commonly reported FBG behavior around 1550 nm (≈1–1.2 pm/με and ≈ 10–14 pm/°C).

Regarding pressure response, it is important to note that reported pressure sensitivities vary widely depending on the transducer design (e.g., diaphragm-based or polymer-enhanced structures can reach tens to hundreds of pm/kPa).

In contrast, the lower range 5–15 pm/kPa predicted here can be expected for configurations where pressure is converted to axial strain through the composite/packaging mechanics and strain-transfer efficiency, which is a known challenge for embedded FBG sensing in composites and a key SHM motivation for improved coupled modeling.

The resolution of the sensor is defined as the minimum detectable change of the measured parameter and is determined by the ratio between the wavelength resolution of the interrogation system and the sensitivity of the FBG sensor.

Assuming a wavelength resolution of the interrogation system of $\delta\lambda\_min = 1$ pm, the resolution for different physical parameters can be estimated as follows.

The obtained resolution values demonstrate that the proposed FBG sensing system is suitable for accurate monitoring of thermo-mechanical effects in composite structures and meets the requirements of structural health monitoring applications.

Although the proposed model and the laboratory-level verification demonstrate

consistent thermo-mechanical behavior of the embedded FBG sensing channel, the present study does not yet include full-scale prototype testing in real operational environments (e.g., aerospace composite panels under service-like thermal cycles or civil engineering elements under long-term loading). Therefore, the claims regarding readiness for deployment in aerospace and civil infrastructure should be interpreted as application potential rather than demonstrated field performance. In future work, we will conduct scenario-driven validation using representative test objects (e.g., a composite coupon/panel with embedded FBGs under combined temperature–pressure/strain cycles and controlled damage introduction), and we will report application-oriented metrics such as measurement resolution, repeatability, drift, and long-term stability under environmental exposure.

4. Conclusion

This study proposed and validated a mathematical model and simulation framework for a fiber-optic sensor system utilizing fiber Bragg gratings (FBGs) embedded in composite materials. The model successfully captures the Bragg wavelength shift caused by both mechanical strain and temperature, enabling accurate dual-parameter sensing. Simulations in MATLAB/Simulink showed that the Bragg wavelength exhibits a linear shift of approximately 1.4 pm/με under axial strain and 10 pm/°C under temperature variation, matching theoretical expectations. The pressure sensitivity of the sensor was found to be in the range of 5–15 pm/kPa, and the refractive index sensitivity reached up to 500 nm/RIU, demonstrating high responsiveness. The spectral range of the sensor was tunable between 1530 and 1570 nm, making it suitable for various applications. The simulations also confirmed that the sensor maintains stable performance under simultaneous variations in pressure and temperature, with an overall reflected power shift pattern closely following experimental measurements. These results confirm that the developed FBG-based sensing system offers a compact, accurate, and reliable solution for structural health monitoring, particularly in aerospace, civil, and industrial environments, where high sensitivity and durability are required. This work validates the model against laboratory measurements; however, real-world prototype testing in aerospace and civil-engineering scenarios is beyond the scope of the present paper. Future work will include scenario-based validation on representative composite structures and reporting deployment metrics (resolution, repeatability, drift, and long-term stability).

Author contributions: AK (Aliya Kalizhanova) and AK (Ainur Kozbakova)—conceptualization and supervision; MK—investigation, software, and resources; AK (Aliya Kalizhanova), AK (Ainur Kozbakova), and MK—validation and data processing; AK (Aliya Kalizhanova)—project administration; FM—visualization and manuscript editing; TK—methodology and formal analysis. All authors have read and agreed to the published version of the manuscript.

Funding: This research is funded by the Science Committee of the Ministry of Science and Higher Education of the Republic of Kazakhstan (Grant No. AP AP32729759).

Institutional review board statement: Not applicable.

Informed consent statement: Not applicable.

Data availability statement: No new experimental dataset was created in this study. All results were obtained from MATLAB/Simulink simulations based on the model structure, equations, and parameter ranges described in the Methods section. The simulation configuration (block parameters, initial conditions, and input scenarios) and representative output files generated during the study are available from the corresponding author upon reasonable request.

Acknowledgment: Many thanks for the financial support of the Ministry of Science and Higher Education of the Republic of Kazakhstan within the framework of the project No. AP19679153, CSMSHE Institute of Information and Computing Technologies of the Republic of Kazakhstan.

Conflict of interest: The authors declare no conflict of interest.

References

1. Xian G, Guo R, Li C. Combined effects of sustained bending loading, water immersion and fiber hybrid mode on the mechanical properties of carbon/glass fiber reinforced polymer composite. Composite Structures. 2022; 281: 115060. doi: 10.1016/j.compstruct.2021.115060
2. Das TK, Ghosh P, Das NC. Preparation, development, outcomes, and application versatility of carbon fiber-based polymer composites: a review. Advanced Composites and Hybrid Materials. 2019; 2(2): 214–233. doi: 10.1007/s42114-018-0072-z
3. Kalizhanova A, Kozbakova A, Kunelbayev M, et al. Sensor Systems for Measuring Force and Temperature with Fiber-Optic Bragg Gratings Embedded in Composite Materials. Journal of Composites Science. 2024; 8(8): 321. doi: 10.3390/jcs8080321
4. Akman F, Ogul H, Ozkan I, et al. Study on gamma radiation attenuation and non-ionizing shielding effectiveness of niobium-reinforced novel polymer composite. Nuclear Engineering and Technology. 2022; 54(1): 283–292. doi: 10.1016/j.net.2021.07.006
5. Ramadan W, Sakr K, Sayed M, et al. Investigation of acrylic/boric acid composite gel for neutron attenuation. Nuclear Engineering and Technology. 2020; 52(11): 2607–2612. doi: 10.1016/j.net.2020.04.014
6. Jang J-H, Hong S-B, Kim J-G, et al. Accelerated Testing Method for Predicting Long-Term Properties of Carbon Fiber-Reinforced Shape Memory Polymer Composites in a Low Earth Orbit Environment. Polymers. 2021; 13(10): 1628. doi: 10.3390/polym13101628
7. Wang L, Zhang F, Liu Y, et al. γ-rays radiation resistant shape memory cyanate ester resin and its composites with high transition temperature. Smart Materials and Structures. 2019; 28(7): 075039. doi: 10.1088/1361-665X/ab2559
8. Nishida M, Hongo A, Hiraiwa Y, et al. Effects of gamma ray irradiation on penetration hole in and fragment size from carbon fiber reinforced composite plates in hypervelocity impacts. Composites Part B: Engineering. 2019; 169: 229–238. doi: 10.1016/j.compositesb.2019.04.007
9. Pastore R, Delfini A, Albano M, et al. Outgassing effect in polymeric composites exposed to space environment thermal-vacuum conditions. Acta Astronautica. 2020; 170: 466–471. doi: 10.1016/j.actaastro.2020.02.019
10. Jang JH, Hong SB, Kim J-G, et al. Long-term properties of carbon fiber-reinforced shape memory epoxy/polymer composites exposed to vacuum and ultraviolet radiation. Smart Materials and Structures. 2019; 28(11): 115013. doi: 10.1088/1361-665X/ab3fda
11. Zheng L-F, Wang L-N, Wang Z-Z, et al. Effects of γ-Ray Irradiation on the Fatigue Strength, Thermal Conductivities and Thermal Stabilities of the Glass Fibres/Epoxy Resins Composites. Acta Metallurgica Sinica (English Letters). 2018; 31(1): 105–112. doi: 10.1007/s40195-017-0692-2
12. Sekulic D, Stevanovic MM. Effects of gamma irradiation and post-irradiation annealing on carbon/epoxy UDC properties deduced by methods of local loading. Journal of Nuclear Materials. 2011; 412(1): 190–194. doi:

10.1016/j.jnucmat.2011.01.125
13. Wu ZX, Li JW, Huang CJ, et al. Effect of gamma irradiation on the mechanical behavior, thermal properties and structure of epoxy/glass-fiber composite. Journal of Nuclear Materials. 2013; 441(1–3): 67–72. doi: 10.1016/j.jnucmat.2013.05.041
14. Liu Liangsen, Feng L, Ma T, et al. Mechanical properties, thermal stability and microstructure evolution of carbon fiber-reinforced epoxy composites exposed to high-dose γ-rays. Radiation Physics and Chemistry. 2022; 194: 110056. doi: 10.1016/j.radphyschem.2022.110056
15. Li R, Gu Y, Yang Z, et al. Effect of γ irradiation on the properties of basalt fiber reinforced epoxy resin matrix composite. Journal of Nuclear Materials. 2015; 466: 100–107. doi: 10.1016/j.jnucmat.2015.07.037
16. Hoffman EN, Skidmore TE. Radiation effects on epoxy/carbon-fiber composite. Journal of Nuclear Materials. 2009; 392(2): 371–378. doi: 10.1016/j.jnucmat.2009.03.027
17. Freund I, Rosenbluh M, Feng S. Memory Effects in Propagation of Optical Waves through Disordered Media. Physical Review Letters. 1988; 61(20): 2328–2331. doi: 10.1103/PhysRevLett.61.2328
18. Tzang O, Niv E, Singh S, et al. Wavefront shaping in complex media with a 350 kHz modulator via a 1D-to-2D transform. Nature Photonics. 2019; 13(11): 788–793. doi: 10.1038/s41566-019-0503-6
19. Stasio N, Conkey DB, Moser C, et al. Light control in a multicore fiber using the memory effect. Optics Express. 2015; 23(23): 30532. doi: 10.1364/OE.23.030532
20. Elsarnagawy T, Haueisen J, Farrag M, et al. Embedded Fiber Bragg Grating Based Strain Sensor as Smart Costume for Vital Signal Sensing. Sensor Letters. 2014; 12(11): 1669–1674.
21. Hu Y, Li Yong, Yan D, et al. Strain transfer of fiber Bragg grating sensors in fiber-reinforced polymer composites with different fiber orientations and temperatures. Measurement. 2024; 225: 114005. doi: 10.1016/j.measurement.2023.114005
22. Ye XW, Ni YQ, Yin JH. Safety Monitoring of Railway Tunnel Construction Using FBG Sensing Technology. Advances in Structural Engineering. 2013; 16(8): 1401–1409. doi: 10.1260/1369-4332.16.8.1401
23. Sabapathi T, Aishwarya K, Pavithra M. Tunnel Fire Detection using FBG. International Journal of Engineering Research & Technology. 2020; 9(3). doi: 10.17577/IJERTV9IS030106
24. Boateng EKG, Schubel P, Umer R. Thermal isolation of FBG optical fibre sensors for composite cure monitoring. Sensors and Actuators A: Physical. 2019; 287: 158–167. doi: 10.1016/j.sna.2019.01.001
25. Schubel P, Umer R, Boateng EKG. Modelling heat transfer through an FBG optical fibre. Composites Part A: Applied Science and Manufacturing. 2018; 109: 184–196. doi: 10.1016/j.compositesa.2018.02.031
26. Kalizhanova A, Kunelbayev M, Kozbakova A, et al. Computation of temperature, deformation and pressure in engineering and building structures using fiber Bragg sensor with tilted grating in Kazakhstan. Materials Today: Proceedings. 2022; 50: 1333–1340. doi: 10.1016/j.matpr.2021.08.252
27. Her S-C, Lin W-N. Simultaneous Measurement of Temperature and Mechanical Strain Using a Fiber Bragg Grating Sensor. Sensors. 2020; 20(15): 4223. doi: 10.3390/s20154223
28. Kashaganova G, Kozbakova A, Kartbayev T, et al. Research of a Fiber Sensor Based on Fiber Bragg Grating for Road Surface Monitoring. Electronics. 2023; 12(11): 2491. doi: 10.3390/electronics12112491
29. Kiesewetter D, Krivosheev S, Magazinov S, et al. Application of Fiber Bragg Gratings as a Sensor of Pulsed Mechanical Action. Sensors. 2022; 22(19): 7289. doi: 10.3390/s22197289
30. Fernández MP, Bulus Rossini LA, Cruz JL, et al. High-speed and high-resolution interrogation of FBG sensors using wavelength-to-time mapping and Gaussian filters. Optics Express. 2019; 27(25): 36815. doi: 10.1364/OE.27.036815
31. Zhang B, Li Z, Wu H, et al. Research on damping performance and strength of the composite laminate. Scientific Reports. 2021; 11(1): 18281. doi: 10.1038/s41598-021-97933-w